

8-27-2012

Direct fabrication of silicon photonic devices on a flexible platform and its application for strain sensing

Li Fan

Birck Nanotechnology Center, Purdue University, lfan@purdue.edu

Leo T. Varghese

Birck Nanotechnology Center, Purdue University, vleotom@purdue.edu

Yi Xuan

Birck Nanotechnology Center, Purdue University, yxuan@purdue.edu

Jian Wang

Birck Nanotechnology Center, Purdue University, wang381@purdue.edu

Ben Niu

Birck Nanotechnology Center, Purdue University, bniu@purdue.edu

See next page for additional authors

Follow this and additional works at: <http://docs.lib.purdue.edu/nanopub>



Part of the [Nanoscience and Nanotechnology Commons](#)

Fan, Li; Varghese, Leo T.; Xuan, Yi; Wang, Jian; Niu, Ben; and Qi, Minghao, "Direct fabrication of silicon photonic devices on a flexible platform and its application for strain sensing" (2012). *Birck and NCN Publications*. Paper 1147.
<http://dx.doi.org/10.1364/OE.20.020564>

Authors

Li Fan, Leo T. Varghese, Yi Xuan, Jian Wang, Ben Niu, and Minghao Qi

Direct fabrication of silicon photonic devices on a flexible platform and its application for strain sensing

Li Fan,* Leo T. Varghese, Yi Xuan, Jian Wang, Ben Niu, and Minghao Qi

School of Electrical and Computer Engineering, Birck Nanotechnology Center, Purdue University, West Lafayette, IN 47906, USA
*lfan@purdue.edu

Abstract: We demonstrate a process to fabricate silicon photonic devices directly on a plastic film which is both flexible and transparent. This process allows the integration of complex structures on plastic films without the need of transferring from another substrate. Waveguides, grating couplers, and microring resonators are fabricated and optically characterized. An optical strain sensor is shown as an application using 5 μm -radius microring resonators on the flexible substrate. When strain is applied, resonance wavelength shifts of the microring resonators are observed. Contributions of different effects are analyzed and evaluated. Finally, we measure the influence of residual strain and confirm the material undergoes elastic deformation within the applied strain range.

©2012 Optical Society of America

OCIS codes: (220.4000) Microstructure fabrication; (220.4241) Nanostructure fabrication; (130.3120) Integrated optics devices; (280.4788) Optical sensing and sensors; (160.1050) Acousto-optical materials; (120.4880) Optomechanics.

References and links

1. M. H. Khan, H. Shen, Y. Xuan, L. Zhao, S. J. Xiao, D. E. Leaird, A. M. Weiner, and M. H. Qi, "Ultrabroad-bandwidth arbitrary radiofrequency waveform generation with a silicon photonic chip-based spectral shaper," *Nat. Photonics* **4**(2), 117–122 (2010).
2. L. Fan, J. Wang, L. T. Varghese, H. Shen, B. Niu, Y. Xuan, A. M. Weiner, and M. H. Qi, "An all-silicon passive optical diode," *Science* **335**(6067), 447–450 (2012).
3. F. Cavallo and M. G. Lagally, "Semiconductors turn soft: inorganic nanomembranes," *Soft Matter* **6**(3), 439–455 (2010).
4. D.-H. Kim and J. A. Rogers, "Bend, buckle, and fold: mechanical engineering with nanomembranes," *ACS Nano* **3**(3), 498–501 (2009).
5. D. H. Kim, J. H. Ahn, W. M. Choi, H. S. Kim, T. H. Kim, J. Z. Song, Y. Y. Huang, Z. J. Liu, C. Lu, and J. A. Rogers, "Stretchable and foldable silicon integrated circuits," *Science* **320**(5875), 507–511 (2008).
6. J. A. Rogers, M. G. Lagally, and R. G. Nuzzo, "Synthesis, assembly and applications of semiconductor nanomembranes," *Nature* **477**(7362), 45–53 (2011).
7. S. R. Quake and A. Scherer, "From micro- to nanofabrication with soft materials," *Science* **290**(5496), 1536–1540 (2000).
8. S. Ashkenazi, C. Y. Chao, L. J. Guo, and M. O'Donnell, "Ultrasound detection using polymer microring optical resonator," *Appl. Phys. Lett.* **85**(22), 5418–5420 (2004).
9. B. Bhola and W. H. Steier, "A novel optical microring resonator accelerometer," *IEEE Sens. J.* **7**(12), 1759–1766 (2007).
10. J. K. S. Poon, L. Zhu, G. A. DeRose, and A. Yariv, "Polymer microring coupled-resonator optical waveguides," *J. Lightwave Technol.* **24**(4), 1843–1849 (2006).
11. B. Bhola, H. C. Song, H. Tazawa, and W. H. Steier, "Polymer microresonator strain sensors," *IEEE Photon. Technol. Lett.* **17**(4), 867–869 (2005).
12. D. Chanda, K. Shigeta, S. Gupta, T. Cain, A. Carlson, A. Mihi, A. J. Baca, G. R. Bogart, P. Braun, and J. A. Rogers, "Large-area flexible 3D optical negative index metamaterial formed by nanotransfer printing," *Nat. Nanotechnol.* **6**(7), 402–407 (2011).
13. W. D. Zhou, Z. Q. Ma, H. J. Yang, Z. X. Qiang, G. X. Qin, H. Q. Pang, L. Chen, W. Q. Yang, S. Chuwongin, and D. Y. Zhao, "Flexible photonic-crystal Fano filters based on transferred semiconductor nanomembranes," *J. Phys. D Appl. Phys.* **42**(23), 234007 (2009).
14. D. Taillaert, W. V. Paepegeem, J. Vlekken, and R. Baets, "A thin foil optical strain gage based on silicon-on-insulator microresonators," *Proc. SPIE* **6619**, 661914, 661914-4 (2007).

15. J. Yoon, L. F. Li, A. V. Semichaevsky, J. H. Ryu, H. T. Johnson, R. G. Nuzzo, and J. A. Rogers, "Flexible concentrator photovoltaics based on microscale silicon solar cells embedded in luminescent waveguides," *Nat Commun* **2**, 343 (2011).
16. D.-H. Kim, N. Lu, R. Ghaffari, and J. A. Rogers, "Inorganic semiconductor nanomaterials for flexible and stretchable bio-integrated electronics," *NPG Asia Mater.* **4**(4), e15 (2012).
17. S. K. Selvaraja, P. Jaenen, W. Bogaerts, D. Van Thourhout, P. Dumon, and R. Baets, "Fabrication of Photonic Wire and Crystal Circuits in Silicon-on-Insulator Using 193-nm Optical Lithography," *J. Lightwave Technol.* **27**(18), 4076–4083 (2009).
18. W. Bogaerts, P. Dumon, D. Taillaert, V. Wiaux, S. Beckx, B. Luyssaert, J. Van Campenhout, D. Van Thourhout, and R. Baets, "SOI nanophotonic waveguide structures fabricated with deep UV lithography," *Photon. Nano. Fund. Appl.* **2**(2), 81–86 (2004).
19. U. Plachetka, N. Koo, T. Wahlbrink, J. Bolten, M. Waldow, T. Plotzing, M. Forst, and H. Kurz, "Fabrication of photonic ring resonator device in silicon waveguide technology using soft UV-nanoimprint lithography," *IEEE Photon. Technol. Lett.* **20**(7), 490–492 (2008).
20. W. J. Westerveld, J. Pozo, P. J. Harmsma, R. Schmits, E. Tabak, T. C. van den Dool, S. M. Leinders, K. W. A. van Dongen, H. P. Urbach, and M. Yousefi, "Characterization of a photonic strain sensor in silicon-on-insulator technology," *Opt. Lett.* **37**(4), 479–481 (2012).
21. Y. Amemiya, Y. Tanushi, T. Tokunaga, and S. Yokoyama, "Photoelastic effect in silicon ring resonators," *Jpn. J. Appl. Phys.* **47**(4), 2910–2914 (2008).
22. A. Harke, M. Krause, and J. Mueller, "Low-loss singlemode amorphous silicon waveguides," *Electron. Lett.* **41**(25), 1377–1379 (2005).
23. S. K. Selvaraja, E. Sleckx, M. Schaekers, W. Bogaerts, D. Van Thourhout, P. Dumon, and R. Baets, "Low-loss amorphous silicon-on-insulator technology for photonic integrated circuitry," *Opt. Commun.* **282**(9), 1767–1770 (2009).
24. S. Y. Zhu, G. Q. Lo, and D. L. Kwong, "Low-loss amorphous silicon wire waveguide for integrated photonics: effect of fabrication process and the thermal stability," *Opt. Express* **18**(24), 25283–25291 (2010).
25. R. Sun, K. McComber, J. Cheng, D. K. Sparacin, M. Beals, J. Michel, and L. C. Kimerling, "Transparent amorphous silicon channel waveguides with silicon nitride intercladding layer," *Appl. Phys. Lett.* **94**(14), 141108 (2009).
26. T. Barwicz and H. A. Haus, "Three-dimensional analysis of scattering losses due to sidewall roughness, in microphtonic waveguides," *J. Lightwave Technol.* **23**(9), 2719–2732 (2005).
27. D. Taillaert, W. Bogaerts, P. Bienstman, T. F. Krauss, P. Van Daele, I. Moerman, S. Verstuyft, K. De Mesel, and R. Baets, "An out-of-plane grating coupler for efficient butt-coupling between compact planar waveguides and single-mode fibers," *IEEE J. Quantum Electron.* **38**(7), 949–955 (2002).
28. Y. B. Tang, D. X. Dai, and S. L. He, "Proposal for a Grating Waveguide Serving as Both a Polarization Splitter and an Efficient Coupler for Silicon-on-Insulator Nanophotonic Circuits," *IEEE Photon. Technol. Lett.* **21**(4), 242–244 (2009).
29. L. B. Freund and S. Suresh, *Thin Film Materials: Stress, Defect Formation, and Surface Evolution* (Cambridge University Press, Cambridge, UK; New York, 2003).
30. O. Renner and J. Zemek, "Density of amorphous silicon films," *Czech. J. Phys. B* **23**, 1273–1276 (1973).
31. D. J. McClure, "Polyester (PET) Film as a Substrate: A Tutorial," in *Proceedings of the 50th Annual Technical Conference of the Society of Vacuum Coaters* (2007), pp. 692–699 (2007).
32. W. Bogaerts, P. De Heyn, T. Van Vaerenbergh, K. De Vos, S. Kumar Selvaraja, T. Claes, P. Dumon, P. Bienstman, D. Van Thourhout, and R. Baets, "Silicon microring resonators," *Laser Photon. Rev.* **6**(1), 47–73 (2012).
33. S. G. Johnson and J. D. Joannopoulos, "Block-iterative frequency-domain methods for Maxwell's equations in a planewave basis," *Opt. Express* **8**(3), 173–190 (2001).
34. H. Gleskova and S. Wagner, "Amorphous silicon thin-film transistors on compliant polyimide foil substrates," *IEEE Electron Device Lett.* **20**(9), 473–475 (1999).
35. Z. Suo, E. Y. Ma, H. Gleskova, and S. Wagner, "Mechanics of rollable and foldable film-on-foil electronics," *Appl. Phys. Lett.* **74**(8), 1177–1179 (1999).

1. Introduction

Integrated silicon photonics is an emerging field that aims to miniaturize optical devices and systems, as well as to take advantage of low-cost manufacturing through well-established fabrication technology of complementary metal-oxide-semiconductor (CMOS) devices. It is a promising solution to ultra-broad bandwidth interconnects required in future electronic systems, and can also provide various sensing and transmission functionalities [1, 2]. Photonic devices such as waveguides, resonator cavities, grating couplers, *etc.* are normally realized on rigid platform such as a silicon wafer. Recent studies on semiconductor nanomembranes show that when material dimensions are shrunk to nanometer scale, it is possible to transform brittle semiconductors into "soft" flexible materials, while maintaining its bulk properties [3–6]. The demonstration of a variety of flexible integrated circuits in the

past few years further intrigues the realization of flexible silicon photonic devices for practical applications.

Organic polymer, with its intrinsic characteristic to deform under stress and other properties such as low refractive index and tailorble thickness, provides a good substrate for flexible photonic devices [7]. Polymers have also been used to guide light and functional optical sensing devices such as strain sensor, accelerometer and ultrasound detector have been realized [8–11]. However, inorganic materials such as silicon, metal and III-V semiconductor materials have unique optical properties which cannot be replaced by polymers. For example, most semiconductor materials have a very high refractive index compared to polymeric materials, which helps to make devices with a much smaller footprint. Moreover, semiconductors are generally more robust in harsh operating environments.

How to integrate inorganic and rigid materials on a flexible substrate is of critical importance to realize practical functional devices. Currently, the method used by several groups is to pattern devices on a solid substrate and then transfer the patterned devices to a flexible substrate in the last step [12–15]. The advantage of this strategy is that it allows the fabrication of devices on platforms that have been well understood. However, the transferring step can have limitations such as restricted device area and geometry, sensitivity to bonding surface and usage of sacrificial substrates. Moreover, it introduces additional processing steps, and in some cases specialized techniques or setups are required to achieve good alignment or large-area devices transfer [16].

In this work, we develop a process to directly fabricate amorphous silicon photonic devices on a flexible and transparent plastic substrate. It has the advantage of having fast turn-around time and requiring no special setups. Although electron beam lithography (EBL) is used here, it can be replaced by more cost-effective lithography methods such as deep-UV stepper [17, 18] or nanoimprint lithography [19] (under the thermal budget) in order to achieve low-cost fabrication. Various silicon photonic devices such as microring resonators and grating couplers are fabricated and optically characterized.

An optical based strain sensor is also demonstrated by utilizing the mechanical flexibility of the substrate. We are able to induce strain by bending the plastic film. Compared to long racetracks fabricated on rigid silicon substrates reported [20, 21], we choose 5 μm -radius ring resonators not only because of its smaller footprint, but also because it is circular shape makes it isotropic in detecting strain from any directions on the surface. *In situ* wavelength shifts of microrings under bending stress are characterized. A mechanical model is built to calculate the ring deformation during bending. We then analyze the effects contributing to the resonance wavelength shift under strain. Finally, to our knowledge, the influence of residual strain is evaluated for the first time and results show that the silicon waveguide is elastic within the applied strain range.

2. Fabrication process

There are several challenges in directly integrating silicon devices on flexible substrates. First, the mechanical properties of most conventional polymers depend strongly on temperature and undergo dramatic changes at high temperature. Hydrogenated amorphous silicon with low optical losses is normally deposited at 300°C to 400°C using plasma enhanced chemical vapor deposition (PECVD) [22–25], at which polydimethylsiloxane (PDMS), a substrate widely adopted for flexible applications, will deform and crack. Second, viscoelastic polymers such as PDMS can have minor variations on surface height due to the polymerization and cross-linking process, which leads to stitching errors in EBL and can result in device failures. Third, it is difficult to handle thin and flexible polymer samples during processing. Solutions to overcome these challenges are presented below in our process.

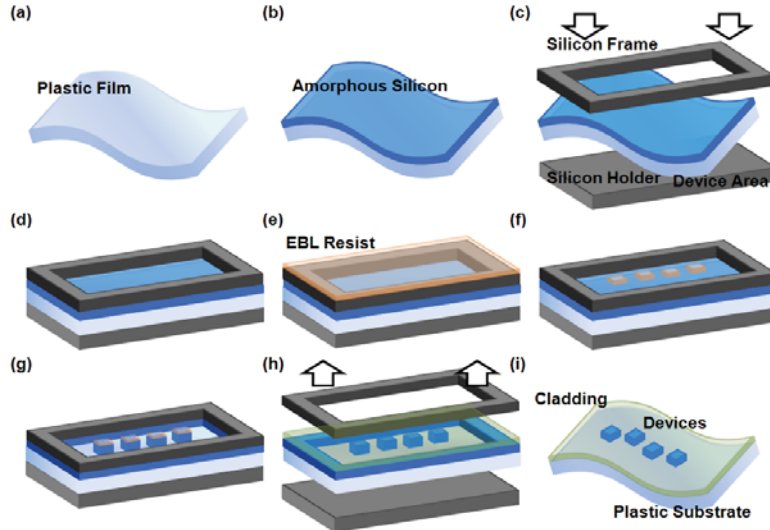


Fig. 1. Direct fabrication process flow. (a) A flexible plastic film is thoroughly cleaned. (b) Amorphous silicon is deposited on top surface using PECVD. (c-d) Sample is sandwiched between two rigid holders. One of them is a silicon wafer, and the other is a silicon wafer with a through-the-wafer opening. (e) Resist is spun over the surface of the sandwiched structure. (f-g) Pattern is written with EBL and etched into silicon with reactive-ion etching (RIE). (h) Surface is overlaid with an index-matching layer and the holders are removed. (i) Free-standing devices without the frame outline.

The direct fabrication process flow is shown in Fig. 1. First, to overcome the thermal budget limitation, we choose a heat stabilized polyester film (Melinex[®], DuPont Teijin Films). With a thickness of $\sim 110 \mu\text{m}$, the plastic film is transparent, flexible yet not stretchable. The refractive index of the plastic film is ~ 1.7 and allows the light to be confined strongly inside the top silicon layer. These attributes make the plastic film a good substrate candidate for silicon photonic devices. To remove particles and organics on the surface, the original film goes through a cleaning process, including solvent clean and piranha (a mixture of sulfuric acid and hydrogen peroxide) clean. The surface has a roughness of about 1.5 nm, measured by atomic force microscopy (AFM), and provides a smooth platform for the material deposition in the next step. Next, we deposit $\sim 270 \text{ nm}$ of amorphous silicon on top of the plastic film using a PECVD tool. Unlike a low pressure chemical vapor deposition tool that deposits amorphous silicon by using decomposing silane to silicon and hydrogen at temperatures above 550°C , a PECVD tool can deposit amorphous silicon at temperatures below 400°C . Since the plastic has a thermal budget of $\sim 250^\circ\text{C}$, we used a temperature of 200°C during deposition which slightly compromises the quality of the silicon film. Nevertheless, relatively smooth films are obtained with a silane flow of 100 sccm (5% diluted in nitrogen) at a pressure of 400 mtorr and an RF power of 25W. The RF power was kept low in order to reduce plasma damage to the film.

The surface roughness of the deposited amorphous silicon is characterized to be about 2.2 nm, which is critical to optical devices so as to minimize the scattering loss caused by surface roughness [26]. After deposition, the sample is sandwiched between two Si substrates with a small window on the top to access the device region (Fig. 1(c) and Fig. 1(d)). This step ensures easy handling of the plastic substrate and also the flatness of the surface over a wide area. Patterns are written by EBL on hydrogen silsesquioxane (HSQ) resist and then transferred to amorphous silicon by reactive ion etching (RIE) (Fig. 1(e) to Fig. 1(g)). After that, a 3 μm -thick layer of polymethyl methacrylate (PMMA) is spun over the whole chip to protect the devices and provide index matching for the grating couplers (Fig. 1(h)). Finally, the plastic film is removed from the silicon holder to be free-standing (Fig. 1(i)).

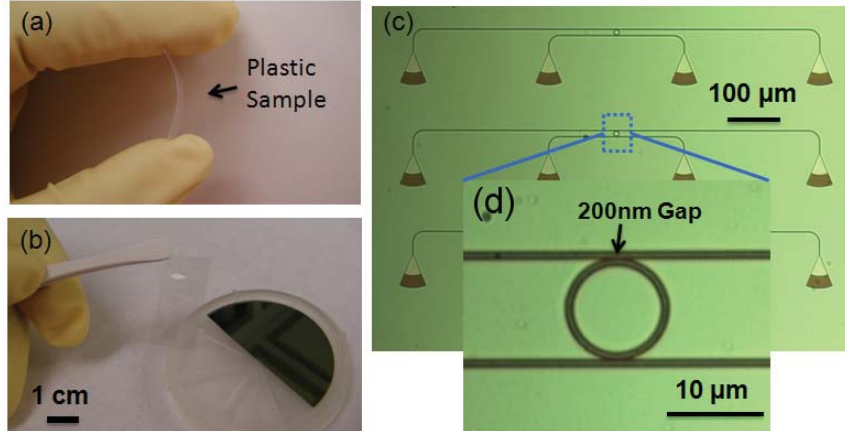


Fig. 2. Optical images of fabricated devices. (a) The plastic sample is held between two fingers to show its mechanical flexibility. (b) The sample is highly transparent in visible spectrum. (c) Amorphous silicon devices under optical microscope. (d) Zoomed-in view of a 5 μm -radius microring resonator.

The fabricated sample (before PMMA overcladding) is shown in Fig. 2(a) and 2(b). It appears flexible and transparent. A number of devices are fabricated on the film and they are nearly invisible to the naked eye. Microscopic image of a typical set of devices is shown in Fig. 2(c). Neighboring grating couplers are separated by about 250 μm . Figure 2(d) shows a zoomed-in view of a 5 μm -radius microring resonator and its coupling waveguides with a gap of 200 nm on both sides. There is no size or shape limit on the patterns that can be realized using the direct fabrication process. Although not shown here, multiple fabrication steps with good alignment can also be accomplished using this process.

3. Measurement setup

Light is coupled in and out of the chip via grating couplers [27]. The grating coupler is designed to have polarization dependent transmission so that majority of the light coupled into the tapered waveguide is of TM polarization [28]. Moreover, the etch depth of the gratings is designed to be the same as the thickness of the amorphous silicon layer so that it can be patterned together with waveguides and rings, without the need for a second lithography and etching step. The coupling loss of the grating coupler is about 8.5 dB per coupler at a wavelength of 1550 nm.

Figure 3(a) shows the setup we designed for optical measurement and strain application. A fiber array with 250 μm spaced fibers is placed ~8 degrees to surface normal. They are mounted on a 5-axis stage so that the relative distance from the sample can be adjusted. This allows us to measure the *in situ* response of the optical devices on the plastic film during bending. A continuous-wave tunable laser source with a wavelength range of 1520 nm to 1620 nm is used as the input. Both edges of the film are taped on a micrometer positioning stage, so that the distance between the two edges of the film can be adjusted quantitatively to induce strain in the silicon microring as it is bent. Figure 3(b) is a picture of the real measurement setup. The device region is transparent, while the brown area is the remaining amorphous silicon that was not etched, outlining the window (Fig. 1(d)) used in the fabrication.

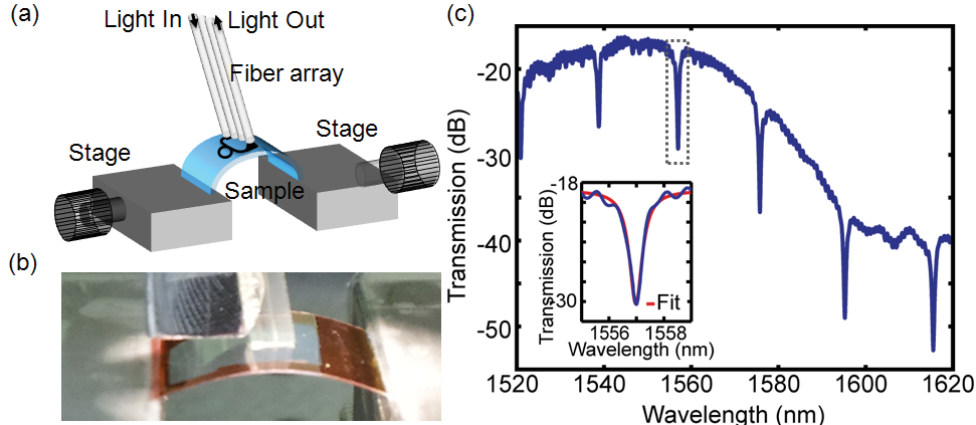


Fig. 3. Measurement setup, strain estimation, and transmission spectrum of a microring device on a flexible substrate. (a) Illustration of the optical measurement setup. Micrometer stages introduce controlled strain onto the sample by bending it upward or downward. (b) Photograph of the real setup. (c) Transmission spectrum of the grating coupler with dips corresponding to the resonance of a 5 μm -radius microring resonator. The inset shows the transmission spectrum (blue) and Lorentzian fitting (red) of the resonance dip near 1550 nm.

To induce strain in the silicon ring, we move the micrometer stage holding the plastic film gradually inwards by a step of 0.25 mm every time and the ring response is recorded each time. The plastic is then allowed to return to its original state by the same stepped movement and the data for the return direction is also recorded.

4. Results and discussion

4.1 Performance of fabricated devices

Figure 3(c) shows a typical transmission spectrum of a device consisting of two grating couplers and a microring resonator. The fabricated grating coupler shows a coupling loss of about 8.5 dB per coupler. The average quality factor of the ring resonators is about 2,000. For comparison, devices of the same parameters are also fabricated on an oxide substrate going through the same process. It is found that the quality factor of the amorphous silicon microring resonators on oxide is about 7000. Compared to reported quality factor of 10,000 for an amorphous silicon racetrack resonator of radius of 4 μm and 180 nm coupling gap on oxide substrate [23], the quality factor of our device on oxide substrate is a little lower probably due to material losses introduced by the low temperature deposition process. The degradation of quality factor for devices on plastic substrate is probably caused by the flexibility of the substrate and the processing condition. Further process optimization will be necessary in order to achieve high quality resonators in the future.

4.2 In situ strain measurement

To understand the strain applied to the microring, let us first analyze the strain on a blanket plastic film during bending. When the plastic is bent up, its top surface experiences tensile stress while its bottom surface experiences compressive stress. The strain on the top surface approximately equals to the distance from the top surface to the midsurface of the film (where there is no strain) divided by the radius of curvature. For a plastic of thickness d and bending radius R , the strain on the top surface is $d/(2R)$. Bending radius R is calculated from measuring the sample geometry in the experiment. Strain has no unit and is generally stated in micro epsilon ($\mu\epsilon$).

Transmissions at different values of strain are measured for microrings on the plastic film. The transmission of one FSR at different surface strain is plotted in Fig. 4(a). The resonance dip of the microring shifts gradually to a longer wavelength with increasing strain. Lorentzian

fitting for each resonance dip is done to accurately locate the resonance wavelength, and the change of resonance wavelength versus strain is plotted in Fig. 4(b). The relationship between resonance wavelength shift and strain is almost linear and a linear fitting shows that the resonance wavelength shift per strain is $0.22 \pm 0.015 \text{ pm}/\mu\epsilon$. Our value is on the same level compared with work reported by Westerveld *et al.*, where a crystalline silicon racetrack on SOI substrate with a length of 1040 μm and a radius of 25 μm shows a resonance wavelength shift per strain of $0.47 \pm 0.04 \text{ pm}/\mu\epsilon$ for 400nm wide waveguide and $0.63 \pm 0.08 \text{ pm}/\mu\epsilon$ for 1000nm wide waveguide [20]. The change in quality factor and extinction ratio at different strain is also plotted in Fig. 5(a) and 5(b) for a typical device. It is clear that neither quality factor or extinction ratio significantly changes under strain.

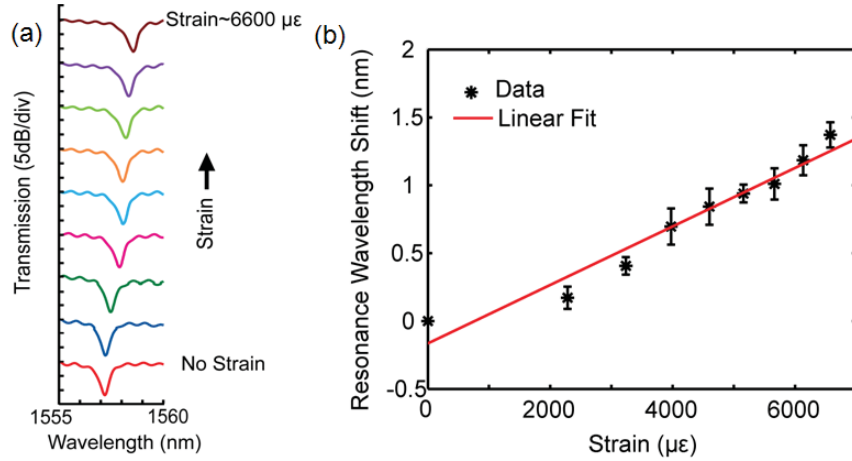


Fig. 4. Resonance wavelength shift under strain. (a) The transmission spectra of a microring resonator at increasing strain are plotted with an offset in y axis. (b) Average and standard deviation of the resonance wavelength shift versus strain. The error bar at each data point is the standard deviation from measuring different samples.

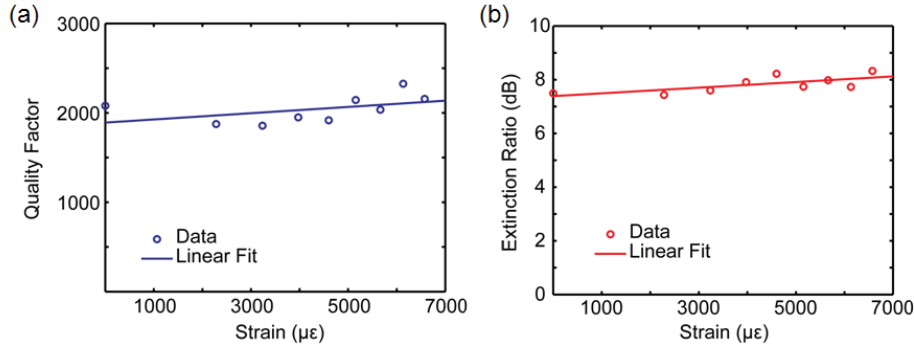


Fig. 5. Change of quality factor and extinction ratio under strain. (a) The quality factor versus strain. (b) The extinction ratio versus strain. Both (a) and (b) are taken at the FSR near 1550 nm for a typical microring device. Linear fittings are plotted to reflect the trend.

The effect of the strain direction is also considered in the experiment. Two identical microring resonators with coupling waveguides in perpendicular directions are made in neighboring positions on the sample. When the same strain is applied, it is along the coupling direction of one ring (inset of Fig. 6(a)) and parallel to the coupling direction of the other ring (inset of Fig. 6(b)). We also measured the cases of increasing strain (bending up) and decreasing strain (bending down), as illustrated in Fig. 6(c). The ring in Fig. 6(a) shows a resonance wavelength shift versus strain of $0.24 \text{ pm}/\mu\epsilon$ when the plastic is bent up and 0.21

$\text{pm}/\mu\epsilon$ when the plastic is bent down. With a standard deviation of $\pm 0.015 \text{ pm}/\mu\epsilon$ from Fig. 4, the two values for bending up and down are within the error of the measurement. The ring in Fig. 6(b) shows a shift versus strain of $0.21 \text{ pm}/\mu\epsilon$ when bent up and $0.20 \text{ pm}/\mu\epsilon$ when bent down. Similarly, the two values are comparable. Moreover, when comparing Fig. 6(a) and Fig. 6(b), the two strain directions have a similar amount of resonance wavelength shift. It is expected because the circular microring resonator is symmetric for both directions, unlike a racetrack, and hence it responds the same way to strain applied in both cases.

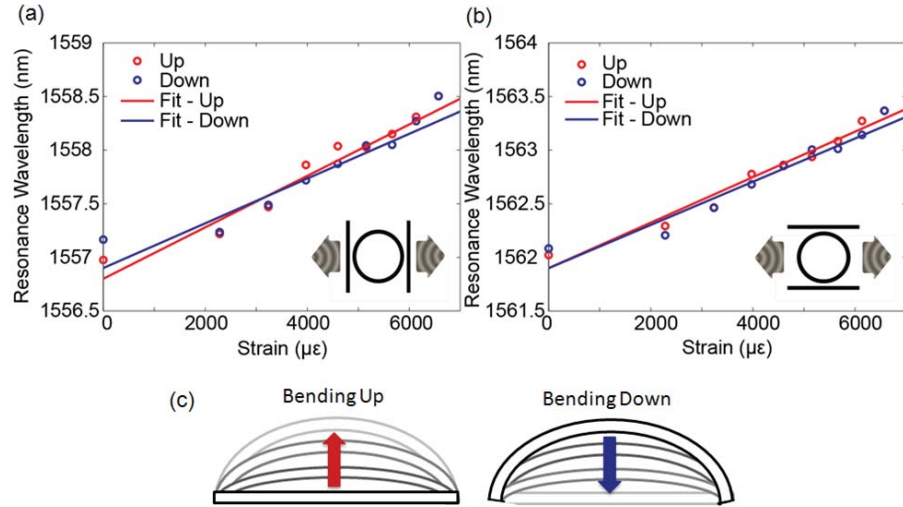


Fig. 6. Effects of strain direction and bending direction. (a) The wavelength shift vs. strain of the microring when strain is applied in the direction along its coupling. (b) The wavelength shift vs. strain when the strain is applied in the perpendicular direction. The insets in (a) and (b) illustrate the direction of applied strain with regard to the device. Circles are measured data points and lines are linear fittings. Red denotes increasing strain (sample bending up) while blue denotes decreasing strain (sample bending down). (c) Side-view illustrations of the sample undergoing bending up and bending down measurements.

4.3 Mechanical deformation of the microring resonator under strain

The geometry change of the device under strain is of critical concern in the analysis. When the plastic film is bent, its surface is under uniaxial tensile strain. The microring deforms not only in the direction along the uniaxial strain but also in the direction perpendicular to the strain axis. Numerical simulations of the three-dimensional deformation of the ring on a bending plastic surface are carried out using Solid Mechanics module by COMSOL Multiphysics. Since the plastic substrate is much larger than the device, only 1 mm by 1 mm size substrate is used in the modeling. The microring dimensions and the plastic thickness are used from the experiment. The material properties for amorphous silicon used in simulation are taken from literature: Young's modulus is 80 GPa [29]; Poisson's ratio is 0.22 [29]; mass density is 2210 kg/m^3 [30]. For the plastic, we use Young's modulus of 4.5 GPa, Poisson's ratio of 0.37 and mass density of 2210 kg/m^3 in the simulation [31]. Figure 7(a) shows the deformation of the system when a force is applied underneath the substrate and causes the plastic to bend up.

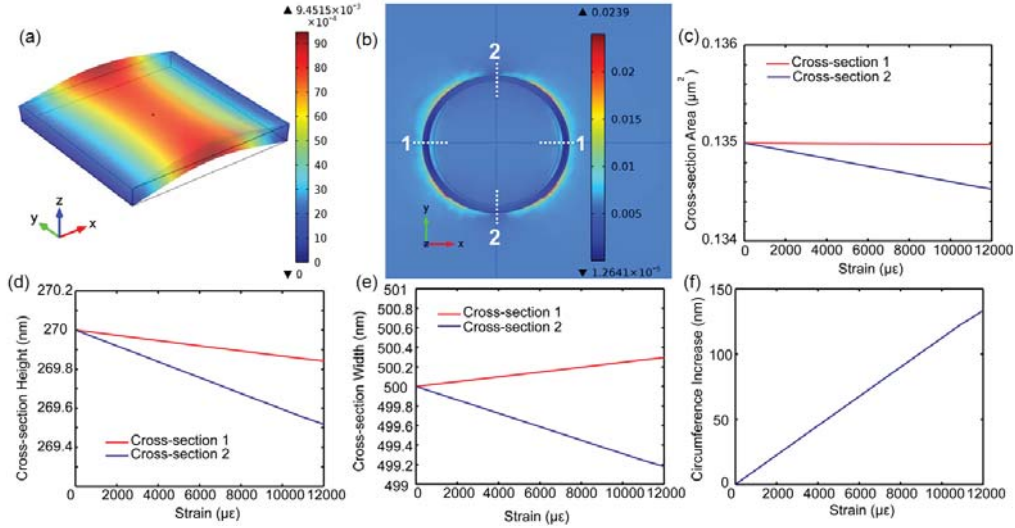


Fig. 7. COMSOL simulation on the deformation of the microring waveguide under strain. (a) The displacement of the substrate under strain. The plastic substrate bends upward and causes deformation of the ring. (b) The strain distribution for the microring and the surrounding area along the uniaxial strain direction (x-direction) obtained from simulation. The calculation shown in the plot corresponds to a surface strain of $\sim 6000 \mu\epsilon$. The four waveguide cross-sections that are parallel to the strain direction (labeled as 1 in the graph) and perpendicular to the strain direction (labeled as 2 in the graph) are of particular interest. The changes in their dimensions (area, height, weight) are examined at different strain values and plotted in (c-f). (f) Increment of the microring circumference versus strain.

The strain distribution in the silicon microring and the surrounding area is shown in Fig. 7(b) along the x-direction, and corresponds to a surface strain of $\sim 6000 \mu\epsilon$. The x-direction is parallel to the direction of the uniaxial strain. The ring is slightly stretched along the x-direction and compressed along the y-direction. Figure 7(c) to Fig. 7(e) plots the simulated cross-section change at various strain values. The two cross-sections perpendicular to the strain, which are labeled as 2 in Fig. 7(b), experience a slight decrease in both height and width under strain: At a strain of $\sim 6000 \mu\epsilon$, the height decreases by ~ 0.3 nm and the width decreases by ~ 0.4 nm. The two cross-sections along the strain direction, which are labeled as 1, shrink slightly in height but expand in width: At a strain of $\sim 6000 \mu\epsilon$, the height decreases by ~ 0.1 nm and the width increases by ~ 0.2 nm. Cross-sectional areas of both these sections decrease when a strain is applied (0.5% for “1” and 0.2% for “2”). The change of the circumference of the microring versus strain is plotted in Fig. 7(f), and it follows a linear relationship. Fitting of the data shows that the influence of strain S on the ring circumference l is $d\ell/dS = 11 \text{ pm}/\mu\epsilon$.

4.4 Effects contributing to the resonance wavelength shift

As discussed in [20], the shift of the resonance wavelength of the microring is mainly due to three effects: Change in ring circumference, shrinkage of waveguide cross section due to Poisson’s effect and the effective refractive index change of the material due to photoelastic effect. For a microring resonator, the condition for resonance is that an integer number of the wavelength of the light needs to match the optical length of the ring:

$$m \cdot \lambda_{\text{res}} = n_e \cdot l \quad \text{where} \quad m = 1, 2, 3, \dots \quad (1)$$

where λ_{res} is the resonance wavelength in vacuum, n_e is the effective index of the guided mode in the microring waveguide and l is the circumference of the microring.

When strain S is applied, it directly alters the circumference l , the effective index of the resonant mode n_e , and the waveguide cross-section dimensions. First, the change of n_e and l changes λ_{res} . Here, the effect of modal dispersion needs to be taken into account because it is a submicron waveguide, and therefore the change of λ_{res} will in turn alter n_e due to the non-zero slope of $\partial n_e / \partial \lambda$. In a first order approximation considering the effect of n_e caused by environmental change as shown in [32], we can decouple the two effects and consider the only first order dispersion.

Second, the change of cross-section will also affect n_e and the group index n_g and change the modal dispersion. To evaluate the effect, we calculate n_e and n_g of microring waveguide with different cross-section dimensions. The simulation is based on eigenmode expansion method, using a freely available software package [33]. It is found that if the cross-section width increases by 10% (from 500 nm to 550 nm), n_e increases by ~1%, n_g increases by ~0.2% and $n_e n_g$ increases by ~1%; if the width decreases by 10% (from 500 nm to 450 nm), n_e decreases by ~3%, n_e decreases by ~1% and $n_e n_g$ decreases by ~2%; if the cross-section height decreases from 270 nm to 250 nm, n_e decreases by ~4%, n_e decreases by ~2% and $n_e n_g$ decreases by ~2%. From the mechanical modeling, at a strain of ~6000 $\mu\epsilon$, the ring waveguide cross-section height decreases by less than 0.3 nm (~0.1%) and the width changes by less than 0.4 nm (~0.1%). Therefore, change of n_e and n_g caused by cross-section change is minimal, and we neglect this effect in the analysis.

With these approximations, the effective index is dependent on both the strain S and the wavelength λ_m . And the circumference l has a dependence on strain S . If we take partial derivatives of Eq. (1) with regard to S , we can get

$$m \frac{\partial \lambda_{res}}{\partial S} = \frac{\partial n_e}{\partial S} l + \frac{\partial n_e}{\partial \lambda_{res}} \frac{\partial \lambda_{res}}{\partial S} l + n_e \frac{\partial l}{\partial S} \quad (2)$$

We solve Eq. (2) for $\partial \lambda_{res} / \partial S$ at the initial state when $l = l_0$ (the circumference of the ring at zero strain) and $\lambda_{res} = \lambda_0$ (the resonance wavelength at zero strain), and substitute m from Eq. (1) and n_g as $n_g = n_e - \lambda(\partial n_e / \partial \lambda)$. We can get

$$\frac{\partial \lambda_{res}}{\partial S} = \frac{n_e}{n_g} \frac{\lambda_0}{l_0} \frac{\partial l}{\partial S} + \frac{\lambda_0}{n_g} \frac{\partial n_e}{\partial S} \quad (3)$$

On the right side of the Eq. (3), the factor n_e / n_g reflects the influence of dispersion, and the first term accounts for the contribution of strain-induced circumference change to the resonance wavelength shift. The second term $\lambda_0 / n_g (\partial n_e / \partial S)$ reflects the contribution of effective index change to the resonance wavelength shift.

The slope of resonance wavelength change versus strain $\partial \lambda_0 / \partial S$ is measured in the experiment as 0.22 ± 0.015 pm/ $\mu\epsilon$. The change of circumference versus strain $\partial l / \partial S$ is obtained by mechanical simulation as $\partial l / \partial S = 11$ pm/ $\mu\epsilon$. n_e and n_g for the original waveguide dimensions are calculated to be 2.12 and 4.34 respectively. Thus, the contribution of circumference change to the resonance wavelength shift is $n_e / n_g \cdot \lambda_0 / l_0 (\partial l / \partial S) = 0.27$ pm/ $\mu\epsilon$. By subtracting the second term from the left side of Eq. (3), the contribution of the refractive index change to the resonance wavelength shift is thus obtained to be $\lambda_0 / n_g (\partial n_e / \partial S) = -0.045 \pm 0.015$ pm/ $\mu\epsilon$.

Comparing the contributions from the two effects, we can see that the strain-induced circumference change causes the resonance to shift to the longer wavelength and the index change causes the resonance to shift to shorter wavelength. The two effects oppose each other, which is consistent with what other works have shown [11, 20, 21].

4.5 Residual strain measurement

Residual strain has never been discussed before, to our best knowledge, either because the optical devices are made from soft stretchable polymer or because the strain is too small to

cause significant changes for waveguides on rigid silicon-on-insulator (SOI) substrate. In our work, the plastic substrate can be easily bent with a bending radius of 5mm. Under such strain, whether the silicon optical devices suffer any damage is difficult to conclude from the *in situ* measurements. Thus, another experiment is carried out to measure the influence of residual strain. The plastic is bent up, held in the position for 30 seconds and then released to its original flat state. The response of a microring is characterized at its original state after each bending and its resonance wavelength is compared with the original one. Here, we have tested strain from $\sim 3000 \mu\text{e}$ up to $\sim 12000 \mu\text{e}$, double the maximum amount applied in the *in situ* measurements.

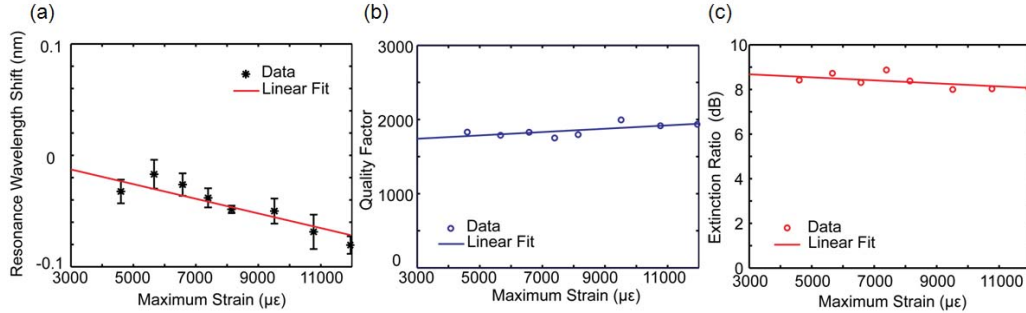


Fig. 8. Effect of residual strain. (a) Resonance wavelength shift with regard to the maximum strain the sample has experienced. Red line gives the linear fit of the shift caused by residual strain. Data are averaged over all the FSRs and error bars are given. (b) Quality factor versus strain. (c) Extinction ratio versus strain. (b) and (c) are taken for a typical device at the FSR near 1550 nm. Linear fitting of the data are drawn to reflect the trend.

The results are shown in Fig. 8. In Fig. 8(a), the resonance shift is smaller than 1% of the *in situ* shifts even with twice as much strain applied to the sample. Linear fitting shows a shift versus strain of $-0.002 \text{ pm}/\mu\text{e}$. This is smaller than the errors between different devices or measurements in the *in situ* case. Figure 8(b) and 8(c) shows that the quality factor and the extinction ratio does not change significantly. Hence, we can conclude that the amorphous silicon device is highly flexible: it has only undergone elastic deformation even under the maximum strain we have applied, and therefore it is safe to neglect the residual strain influences in previous *in situ* experiments. It is found that crystalline silicon nanomembranes are highly bendable compared with the bulk silicon. For example, the mechanical flexural rigidity of a 200-nm-thick silicon membrane is about 10^{11} times smaller than that of a bulk wafer of 200 μm thick [6]. With regard to amorphous silicon, flexible thin-film amorphous silicon transistors have already shown that ~ 250 nm amorphous silicon can be bent to extremely small radii while maintaining its electrical characteristics [34, 35]. Here we demonstrate the flexibility of the amorphous silicon at submicron thickness for optical applications.

5. Conclusions

In summary, we demonstrate a direct fabrication process that can integrate silicon devices onto a flexible polymer substrate, with the advantage of being simple and not requiring any specialized setup. Using this method, amorphous silicon waveguides and microring resonators are successfully fabricated in large numbers on a centimeter-size plastic substrate. Light is coupled in and out of the chip through grating couplers which allow compact footprint and easy access to multiple devices. 5 μm -radius ring resonators are used to detect the strain in the bending sample and microring resonance wavelength shifts at various strains are measured. The strain-induced circumference change is calculated based on 3D mechanical modeling accounting for the plastic and amorphous silicon's physical properties. Different effects contributing to the resonance wavelength shift is analyzed and contributions from the

circumference elongation and refractive index change to the resonance wavelength shift are calculated. Finally, the resonance wavelength shift caused by residual strain is found to be almost negligible, indicating that the amorphous silicon waveguide is elastic and flexible within the strain range.

Acknowledgments

The authors would like to thank Lokesh Gupta for his help in the mechanical modeling. The authors would also like to thank DuPont Inc. for providing the materials. This work was supported by Defense Threat Reduction Agency grant HDTRA1-10-1-0106, Air Force Office of Scientific Research grant FA9550-08-1-0379, and National Science Foundation grants ECCS-0925759, ECCS-0901383 and CNS-1126688.